Wear 520-521 (2023) 204658

Contents lists available at ScienceDirect

Wear

journal homepage: www.elsevier.com/locate/wear

The role of hardening and roughening during the incubation period in water droplet impingement erosion of Ti–6Al–4V

Mohamed Elhadi Ibrahim [a], Mason Marzbali [b], Abdullahi Kachalla Gujba [a], Mamoun Medraj [a,*]

[a] Department of Mechanical, Industrial & Aerospace Engineering, Concordia University, 1455 De Maisonneuve Blvd. W, Montreal, Quebec, H3G 1M8, Canada
[b] Department of Mechanical Engineering, American University in Dubai, P.O. Box 28282, Dubai, United Arab Emirates

ARTICLE INFO

Keywords:
Water droplet erosion
Accumulation of erosion damage
Incubation period
Finite element analysis
Hardening
Surface roughening

ABSTRACT

The present work investigates the role of surface hardening and roughening on the damage accumulation during the incubation period in water droplet erosion (WDE). Water droplet erosion tests were carried out on Ti–6Al–4V alloy at an impact velocity of 250 m/s. The evolution of hardness and surface roughness during the incubation period were evaluated using microhardness tester and Confocal Laser Scanning Microscope (CLSM). Scanning Electron Microscopy (SEM) was conducted on the impact area at several intervals during the incubation period. Finite Element (FE) simulations were performed to obtain the impact stresses on both smooth and rough surfaces. It was found that the solid surface plastically deforms by the action of the initial impingements, and as a result, hardness and surface roughness increase progressively until the end of the incubation period. The cyclic increase in hardness results in gradual improvement in the erosion strength, making the surface more resistant to the subsequent droplet impacts. However, the finite element results revealed that the dynamic surface roughening process results in higher impact stresses for the same impact pressure due to geometrical stress concentration. It is concluded that the increase in impact stresses resulting from surface roughening negates the improvement in the erosion resistance due to hardening. Hence, cyclic hardening and roughening are crucial parameters in the damage accumulation process during the incubation period.

1. Introduction

The gradual loss of material due to repetitive high-speed impingement of water droplets has been a major reliability concern in several power generation components, such as steam turbines [1,2], compressor of gas turbines [3], aero-engine fans [4], and wind turbine blades [5]. The phenomenon is synonymously referred to as Water Droplet Erosion (WDE) [6], Liquid Impingement Erosion (LIE) [7], Leading Edge Erosion (LEE) [8], or Rain Erosion (RE) [9]. WDE damage appears in form of surface pitting that eventually results in imbalance and vibration of rotating components, such as the compressor in gas turbines and the blades of the low pressure stage of steam turbines [5]. As such, understanding the mechanics of WDE damage and predicting its occurrence have been the focus of several recent investigations [1,3,4,6,10–16].

The mechanics of WDE have traditionally been studied under two main tasks; (i) understanding the action of a single impact and (ii) the accumulation of damage due to repetitive impacts. Generally, the collision of a single water drop on a solid surface is a complex dynamic process that involves two main closely phased actions [17,18]; a pressure build-up phase characterized by a peak value (i.e. loading phase), and pressure release phase featured by high velocity lateral outflow as the drop collapses onto the surface (i.e. unloading phase). Both phases are thought to induce stresses in the material. That is, water hammer pressure acts as a direct impact loading parameter that propagates stress waves into the solid and shape its stress and strain fields. Whereas the lateral outflow can potentially exert shear stress on surface irregularities [7,19]. Repetitive impacts on the same area are usually needed to initiate erosion damage, in a way analogous to fatigue [7]. Experimental studies of repetitive WDE have shown that WDE is a time-dependent phenomenon that, with the continuous exposure to droplet impacts, exhibits a nonlinear progression of damage (i.e., different erosion rates at different time intervals [20]). For most of bulk materials, the product of this time dependency is a well-known erosion curve that consists of five different stages of erosion, each has a different erosion rate. Details about the erosion curve and its stages are discussed in Refs. [20,21]. The present work focuses on the first stage which is commonly known as the incubation period. During this period, the repetitive droplet impacts do not - yet - produce any measurable material

* Corresponding author.
E-mail address: mmedraj@encs.concordia.ca (M. Medraj).

https://doi.org/10.1016/j.wear.2023.204658
Received 23 November 2022; Received in revised form 25 January 2023; Accepted 13 February 2023
Available online 14 February 2023

loss. Rather, impact stresses are being accumulated in the material, and only a slight change of surface roughness is observed [17]. The incubation period ends when the stresses have accumulated to a point where further droplet impacts result in local fracture of the material. The fracture is usually observed in the form of small erosion pits and/or the beginning of mass loss from the surface.

The incubation period has been the subject of several investigations [3,22,23] due to the fact that its length largely determines the inherent resistance of the solid surface to water droplet erosion (i.e., erosion strength of the material). Several mechanisms have been proposed to explain the accumulation of damage and the sequence of microscopic events leading to the end of the incubation period. Fatigue, for example, received considerable attention as the principal underlying mechanism responsible for erosion damage accumulation [24,25]. This is mainly due to the repetitive nature of the WDE loading, and the resemblance between the threshold impact velocity (i.e. below which erosion is not likely to occur) and the concept of endurance limit [26]. Incubation prediction models entirely based on fatigue have been developed [23, 25]. However, some researchers argued that fatigue might not be a dominant mechanism in water droplet erosion. For example, Adler's earlier work [17] pointed out, after a closer look at the microstructural damage caused by erosion in metals, that fatigue plays only a secondary role in WDE damage, if any. He suspected that initial impacts are responsible for topological changes in the surface while the damage is caused mainly by lateral jetting and hydraulic penetration. Additionally, fatigue-based models reported in Refs. [23,25] were found to result in very high prediction errors when used to reproduce the experimental incubation period data from the literature [26].

Accumulation of plastic strain leading to fracture of surface fragments has been another hypothesis put forward to explain the course of events during the incubation period. For example, after microscopic observations, Rieger [27] postulated that ductile metals, as an initial response to repetitive droplet impingements, will experience plastic deformation and accumulate plastic strains. After a sufficient number of impingements, a state of deformation is reached, where the density and concentration of dislocations becomes very high. At these locations, the internal stresses exceed the fracture strength of the metal and cracks are formed. Material removal process is then thought of to be through extension and joining of these cracks.

The plastic deformation due to droplet impact results in - and is usually evidenced by - the hardening of impact area. For instance, it was demonstrated in Refs. [26,28] that metals do strain harden by the action of droplet impact before signs of erosion are detected, where hardness was observed to increase until the end of the incubation period. Generally, the hardening process cyclically alters the mechanical properties of the surface, which in turn, control the surface response to subsequent impacts. The dynamic change in the surface properties and its role in the damage accumulation process have never been considered in predicting the incubation period.

Another important factor - yet overlooked in the prediction of the incubation period - is the dynamic change in surface topology caused by the impingement process. Previous studies [15,29] investigated the influence of the initial (starting) surface roughness on the length of incubation period. It was concluded [15] that pre-existing surface irregularities in rough surfaces result in shorter incubation periods compared to that of smooth surfaces. This is because a rough surface puts the material one-step ahead in the damage process by eliminating the roughening stage that constitutes an important part of the incubation period [29]. It is therefore equally important to study the evolution of roughness with time or exposure to droplet impingements and its role on the WDE process [30,31]. This is because different roughening profiles could alter the magnitude and distribution of the impact stress due to variation in stress concentration behavior. As such, the course of the incubation period could be significantly influenced by how the roughness changes with the cyclic droplet impingement.

The present work attempts to address the role of the change in surface condition (i.e., roughening and hardening) on the damage accumulation process during the incubation period. Experimental erosion test is carried out on Ti–6Al–4V, which exhibits impact hardening behavior. Roughness and hardness profiles during the incubation period are evaluated. Finite element analysis is utilized to quantify the stress concentration due to the presence of surface irregularities.

2. Experimental and numerical analysis

2.1. Material

The material selected for this work is the Ti–6Al–4V (ASTM B265, Grade 5) alloy. It is commonly used as a compressor blade material in gas turbines, and is the most studied metallic alloy for water droplet erosion purposes. Sheets of Ti–6Al–4V were received in their annealed condition from Titanium Industries Inc. (Montreal, Canada). The chemical composition of the Ti–6Al–4V alloy is outlined in Table 1, whereas the microstructure of the as-received Ti–6Al–4V samples is shown in Fig. 1. The microstructure consists of equiaxed α grains representing the matrix of the alloy along with uniformly distributed β phase. Some of the basic properties of Ti–6Al–4V relevant to the present work are listed in Table 2.

2.2. Erosion tests

Rotating erosion test rig, shown in Fig. 2, was used to carry out water droplet erosion tests in accordance with ASTM G73 standard [21]. The rig consists of a disc rotating horizontally in a vacuum chamber. Samples are mounted on the periphery of the disc, and water droplets are injected through a nozzle located immediately above the sample. The impact velocity is considered as the linear speed of the rotating disc at the point of impact, which can be varied up to 500 m/s (20,000 rpm).

Samples were cut into test coupons having the dimensions required for the water droplet erosion experiment. The test coupons were then mounted on sample holders (see the sample-holder assembly in Ref. [33]) and attached to the periphery of the rotating disc (as illustrated in Fig. 2). After attaining the desired rotational speed, water was introduced through the nozzle such that the surface of the coupons impacted the droplets at an angle of 90 °, as illustrated in Fig. 3. The test was interrupted at several intervals to examine the impacted area. At each time the test is interrupted, hardness and surface roughness were evaluated before the test is resumed. The test is finalized when the material reaches the end of the incubation period, which is indicated by the appearance of visible erosion pits.

Test parameters used in this study are summarized in Table 3. The 250 m/s impact velocity was chosen because it results in a relatively longer incubation period (>15min). This enables several interruptions (intervals) during the test, which helps in capturing the different microscopic events taking place during the incubation period. The nozzle used in the experiment generates water droplets of varying sizes that are usually represented by a normal distribution, as reported in Mahdipoor et al. [34]. The 600 μm represents the predominant droplet size in the distribution [34], and hence, used in this study to indicate the average droplet size. Furthermore, these droplets lies within the range of droplets impacting the blades of steam turbine and compressor in gas turbine [35,36], which are often made of Ti–6Al–4V. Hence, making the choice of droplet size relevant to real in-service impact conditions.

2.3. Surface characterization

Optical imaging was employed to macroscopically observe the progression of erosion damage during erosion tests. Macrographs of the impact area were obtained at each interruption interval. The impact area was also examined after certain test intervals during the incubation period using Scanning Electron Microscope (SEM, Hitachi S-3400 N). This was done to reveal and measure damage features on the surface as

Table 1
Chemical composition of the Ti–6Al–4V.

Element	Ti	Al	V	Fe	O	C	N	H
Content (wt.%)	87–91	5.5–6.75	3.5–4.5	≤ 0.4	≤ 0.2	≤ 0.08	≤ 0.05	≤ 0.015

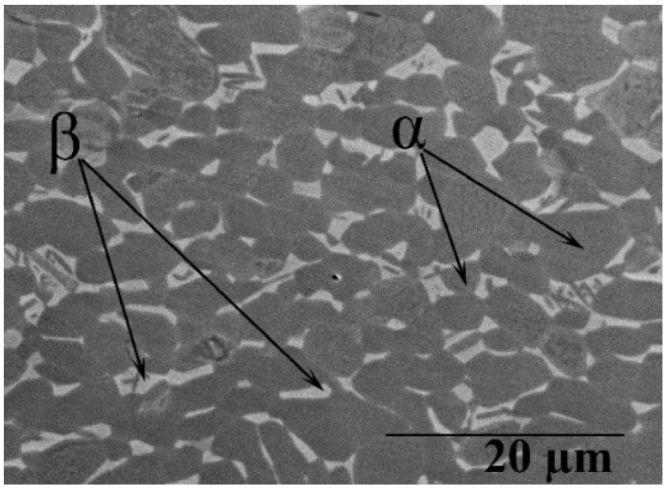

Fig. 1. Microstructure of the as-received Ti–6Al–4V samples.

Table 2
Relevant properties of Ti–6Al–4V at room temperature [32].

Property	Value (unit)
Density	4.43 (g/cm^3)
Speed of Sound	5072 (m/s)
Poisson's Ratio	0.323
Modulus of Elasticity	114 (GPa)
Yield Strength	880 (MPa)
Tensile Strength	950 (MPa)

well as to identify erosion damage mechanisms.

2.4. Hardness measurement

Measurement of surface hardness was carried out using Vickers hardness testing device (Mitutoyo MVK-H1). Load of 300 gf for a holding time of 15 s was utilized. An average of 10 readings was considered for each hardness data point. The initial hardness of the tested coupons was measured before the erosion test. Then, hardness of the impacted area was measured at several intervals to evaluate the hardening process that occurs during the incubation period due to droplet impingements.

To avoid the influence of indentations on the droplet impact process, hardness at each erosion time was measured on different line on the sample. That is, a specific location on the sample was exposed to droplet impacts for 4 min, and then hardness was measured on that location. Then, a different location on the sample was exposed to continuous 8

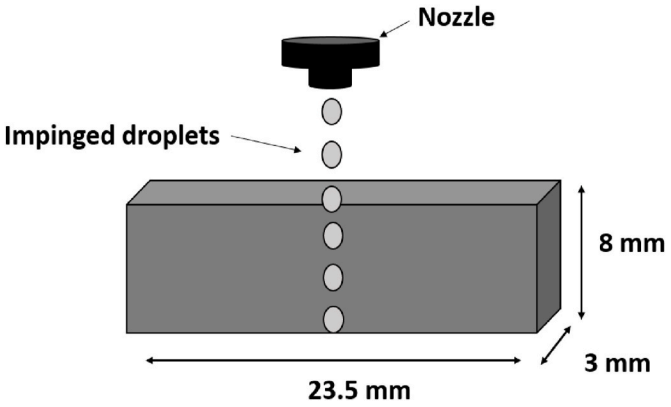

Fig. 3. Sample dimension and the impinged droplets.

Table 3
Erosion test parameters.

Parameter	Value
Impact Velocity (m/s)	250
Average Droplet Size (μm)	600
Impact Angle (degrees)	90
Impact Area (mm^2)	6
Number of impinged droplets per revolution	4

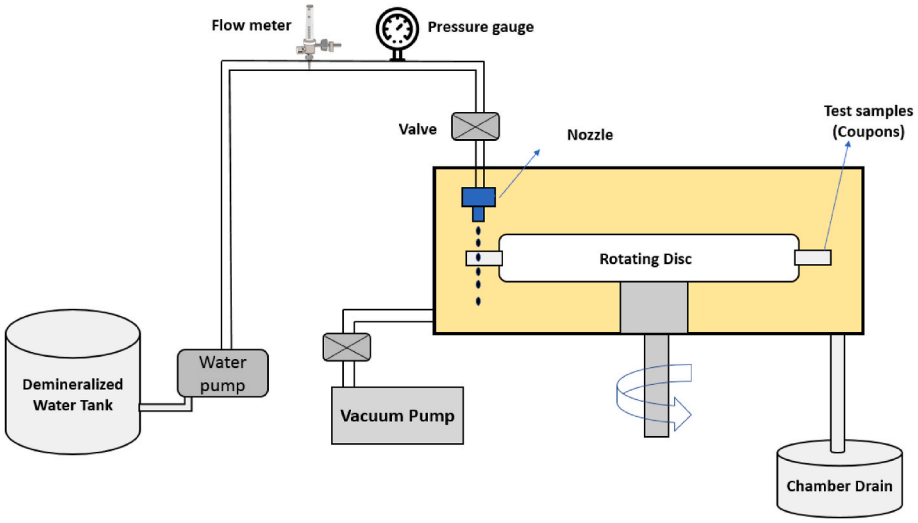

Fig. 2. Erosion test rig at Concordia University.

min of droplet impingements, then hardness was measured. The process was repeated for 12 min and 16 min. In this way, it was ensured that there is no contribution of hardness indentations on the course of the erosion damage, because new impact area is used after the hardness measurement is carried out.

2.5. Roughness measurement

Surface roughness was measured using Confocal Laser Scanning Microscope (CLSM, LEXT-OLS4000, Olympus). CLSM enables a non-destructive scanning of the 3D surface topography, which helps in assessing surface roughness of the tested samples at various intervals during the incubation period. The standard based on which roughness parameters are calculated using the confocal microscope is the ISO 4278 standard.

In this work, at every roughness measurement, the confocal microscope was set to scan an area of $0.5 \times 0.5\ mm^2$, out of which, roughness parameters are calculated. Then, 10 scans were made for each impact line (i.e., erosion duration). The san area of $0.5 \times 0.5\ mm^2$ was selected because it is slightly smaller than the width of the impact area, which ensures that the change in roughness due to droplet impacts is captured. Important roughness parameters such as average surface roughness (Sa) and skewness (Ssk) were first evaluated for the polished samples before the erosion tests. Then, roughness measurements were performed after every WDE test interval, such that the evolution of surface roughness due to droplet impacts was quantified. The use of average surface roughness and skewness is favored due to their consistency in terms of trend seen in the variation of values between each interval during erosion tests [22].

2.6. Numerical analysis

The numerical analysis of water droplet erosion in this work was done in two parts. The first part represents a fluid-solid interaction (FSI) framework that enables the evaluation of the spatial and temporal distribution of the impact pressure (water hammer pressure). In the second part of the analysis, Finite Element Method (FEM) is utilized to obtain the stress-strain field in the solid target that results from the impact pressure. These are detailed in the ensuing discussion.

2.6.1. Spatiotemporal evolution of impact pressure

A Fluid-Solid Interaction (FSI) framework (developed earlier in Refs. [37,38]) has been utilized in this work to obtain the spatiotemporal evolution of impact pressure. The framework consists of compressible Volume of Fluid (VOF) model with a two-dimensional axisymmetric geometry for spherical droplets. It utilizes the ideal gas model for the air and Tait's Equation of State (EOS) for water. Full description as well as the validation of the model can be found in Refs. [37–41].

In the present work, the FSI model was employed to simulate the compressible impact of a 600 μm spherical water droplet impinging a flat rigid surface at a velocity of 250 m/s. The simulation was performed in OpenFoam® software. The obtained spatiotemporal evolution of the impact pressure corresponding to the simulated impact condition is illustrated in Fig. 4.

2.6.2. Finite Element Analysis (FEA)

The impact pressure obtained from the fluid simulation was imported to the finite elements analysis software (ANSYS®) and used as time-step loading boundary condition on the surface of the Ti–6Al–4V sample. The sample (which is shown in Fig. 3) was modeled using the 2D cross section of the coupon (i.e., 8 mm by 3 mm) as illustrated in Fig. 5. Isotropic material properties of Ti–6Al–4V were applied to the 2D model. Then, two-dimensional quadrilateral mesh with a width of 20 μm (30 cells per diameter of the water droplet) was generated in ANSYS® Mechanical for transient structural modelling in Cartesian coordinate system, as shown in Fig. 6. The top 500-μm layer was meshed with square 20-μm elements and a growth rate of 1.015 was applied to the mesh along the depth, from the top surface toward the bottom surface, to reduce the number of total elements (=38000). A grid sensitivity analysis was performed to ensure that further grid refinement does not change the overall maximum stress in the plate. It is worth mentioning that the grid size used in the Computational Fluid Dynamics (CFD) simulations for this case was 1 μm, which is considered very fine. This was done to capture the compressible region in the fluid and the high-pressure emergence due to the ejection of the lateral jets. This requires the imported pressure distribution to be mapped (20 CFD nodes

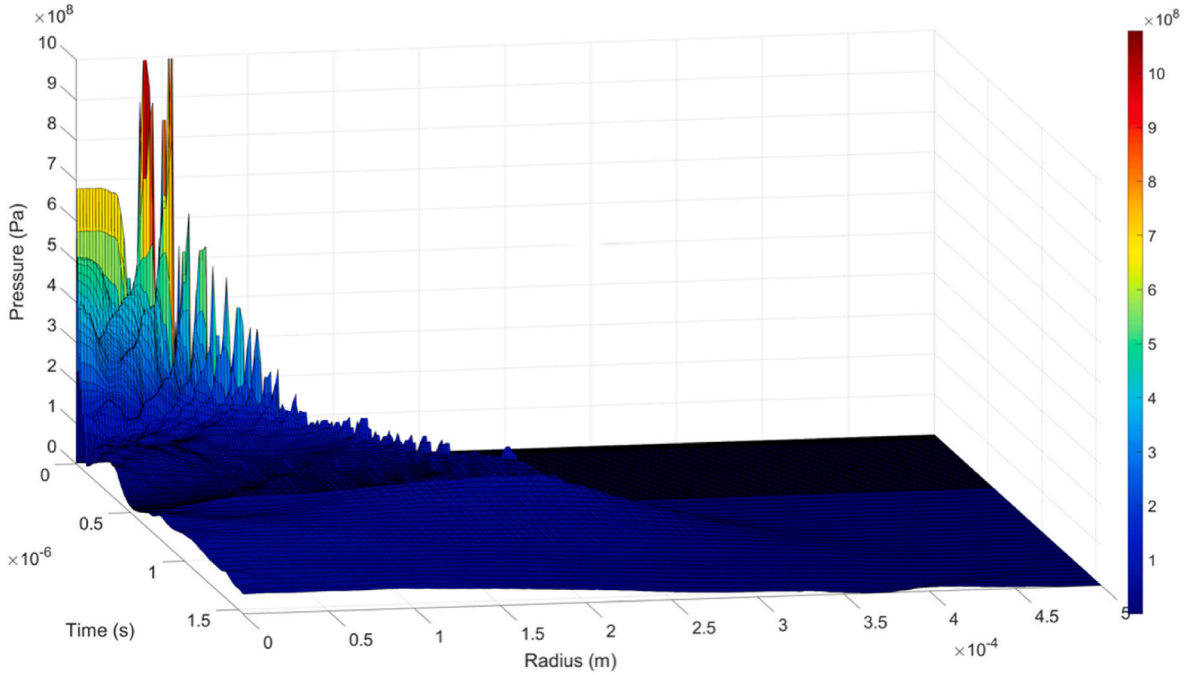

Fig. 4. Spatiotemporal evolution of pressure for a compressible impact of a 600-μm spherical droplet impinging on a flat rigid surface at a velocity of 250 m/s.

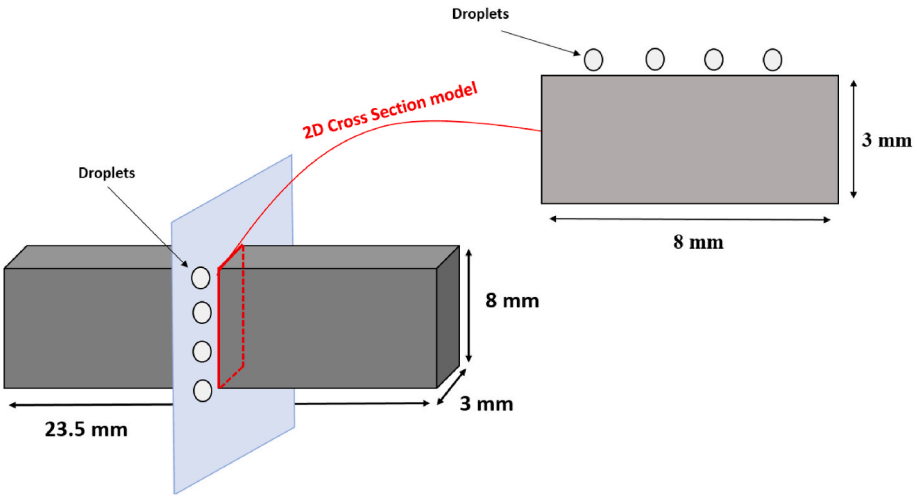

Fig. 5. 2D model for finite element analysis.

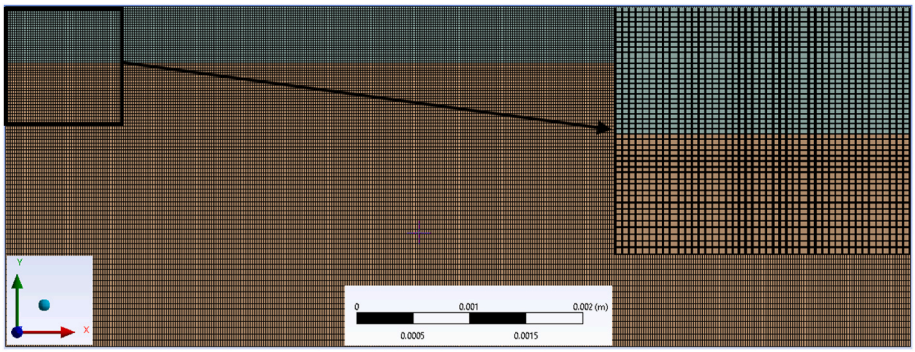

Fig. 6. Two-dimensional quadrilateral mesh used in FEM modelling.

on to 1 FEM node). As such, a mapping with profile preserving and triangulation weighting was applied while importing the pressure load.

Since the length of the coupon (23.5 mm) is much larger than its thickness (3 mm), plane strain condition was applied to the z direction (assuming infinitely long solid bar). Deformation of the solid was set to the elastic mode that follows the Hooke's law. The coupons are assumed to be at room temperature and the heat generated due to the impact is ignored. As such, all thermal stresses are neglected. The imported transient pressure distribution was applied on the top edge. The same impact pressure was applied at four equally-spaced locations on the model to represent the impact conditions of the erosion experiments (as described in Table 3 and Fig. 3). The bottom edge was set to zero displacement (since it is fixed to the coupon holder in the erosion rig). The left and right edges are not constrained and therefore free to deform. The Mechanical APDL solver was used, where Newton-Raphson method was employed for solving the nonlinear equations. Moderate speed dynamics with large deflection was enabled in the solver and an energy dissipation ratio of 10^{-3} was selected. The stiffness coefficient was defined by direct input and both the stiffness and mass coefficients are set to 0. The convergence for force, moment and displacement are all controlled by the program automatically for better stabilization. The simulations were performed on a single processor of a local machine equipped with Intel® Core™ i7-6700 CPU @ 3.40 GHz with 16 GB installed RAM. The average computational time for each case was under 1 h.

Initially, the coupon was modeled as ideal solid material, free of defects and with a flat (smooth) surface. In addition to the flat surface, a series of simulations were performed on a surface containing uniform surface features, as shown in Fig. 7. This was done to simulate the influence of change in surface topology (i.e., presence of surface depression) on the magnitude of the impact stresses. In this regard, 9 cases of uniformly distributed surface depression each having a rectangular shape have been considered. The dimension of the simulated depressions are listed in Table 4. The dimensions have been varied in such way that the influence of width and depth of surface roughness is studied. The size scale of the depression has been approximated from SEM micrographs taken at different intervals during the incubation period.

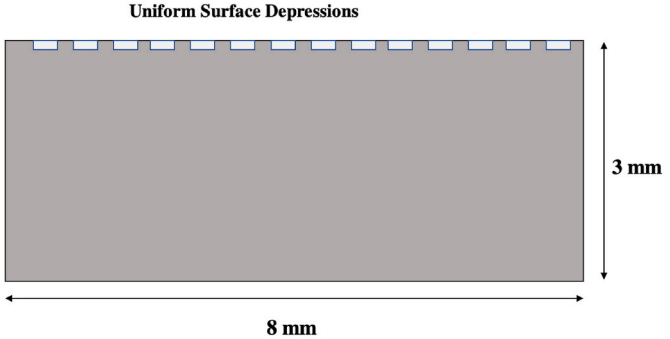

Fig. 7. Illustration of the surface depression; (a) model of uniform surface depression and (b) SEM micrographs of depression.

Table 4
Simulations performed in the finite element analysis.

SIMULATION #	DESCRIPTION	WIDTH (μM)	DEPTH (μM)
1	Flat (smooth) surface		
2	Uniform surface depression (1)	10	10
3		10	20
4		10	30
5	Uniform surface depression (2)	20	10
6		20	20
7		20	30
8	Uniform surface depression (3)	30	10
9		30	20
10		30	30

3. Results

3.1. Erosion behavior and damage mechanisms

Fig. 8 (a) shows the erosion curve of the tested Ti–6Al–4V alloy in which the cumulative material loss (in terms of mass loss in grams) is plotted against cumulative exposure duration (in terms of time in minutes). It is worth noting that the level of repeatability of the WDE tests has been established by Gujba et al. [42] where well-behaved erosion curves at 250 and 350 m/s were generated for Ti–6Al–4V. Images of the Ti–6Al–4V samples at different intervals during the erosion test are shown in Fig. 8 (b). The erosion line, representing the impacted area, can be seen in each image. The appearance of the line indicates that the material is still in the incubation period. The end of the incubation period in this work is considered as the time (or number of impacts) at which uniform erosion pitting appears on the impacted area. This also corresponds to a mass loss of 0.1 mg, which has historically been standardized as the criterion to mark the end of the incubation and was used in Refs. [3,15,33,34]. According to Fig. 8, the end of the incubation period occurs after 16 min of continuous exposure to droplets impacts.

Fig. 9 shows SEM micrographs of the impact area at different intervals during the incubation period of Ti–6Al–4V. The interaction between water droplets and Ti–6Al–4V surface leading to WDE damage at the end of the incubation period can be interpreted as follows. Initial droplet impacts (up to 4 min of exposure) seem to have little effects on the topography of surface of the alloy, where the surface remains relatively smooth and unaffected. During this stage, the surface seems to absorb the kinetic energy of the impacting droplet and plastically deforms. The magnitude of plastic deformation at the early stage of erosion initiation can be deduced from surface hardening in the impact area. After 8 min of exposure, further droplet impingements result in indentations on the surface, as shown in Fig. 9 (b). These indentations are often recognized in the erosion of ductile metals and commonly referred to as surface depressions [3,43,44]. The appearance of surface depressions seems to be accompanied by networks of localized cracks. These cracks potentially stem from the deformation of the β phase causing its separation from the matrix of the Ti–6Al–4V alloy, as suggested in Refs. [45,46]. These surface depressions cause an increase in the overall surface roughness of the alloy, which in turn influences the erosion process.

As the end of the incubation period is approached, erosion pits develop on the surface of the alloy, as shown in Fig. 9 (c) and (d). Erosion pits may initiate from the coalescence of microvoids in the surface and intense cracking. Moreover, traces of tunneling process can be seen inside the erosion pits. This tunneling process accelerates erosion damage as large chunks of materials are removed from the inside and the periphery of the erosion pits, as shown in Fig. 9 (c). The tunneling process is enhanced by the brittle fracture of the β phase within the pits along with the increased formation of localized cracking within the grains, as can be supported by the work of Huang et al. [46]. As the exposure to droplet impacts continues, these tunnels deepen. The intense impact pressures within the tunnels seem to bend the overlying material at the edge of pits, resulting in material upheaval, as shown in Fig. 9 (d). Surface upheavals are likely to be removed or washed away by lateral jetting from subsequent impacts. Hence, the end of incubation

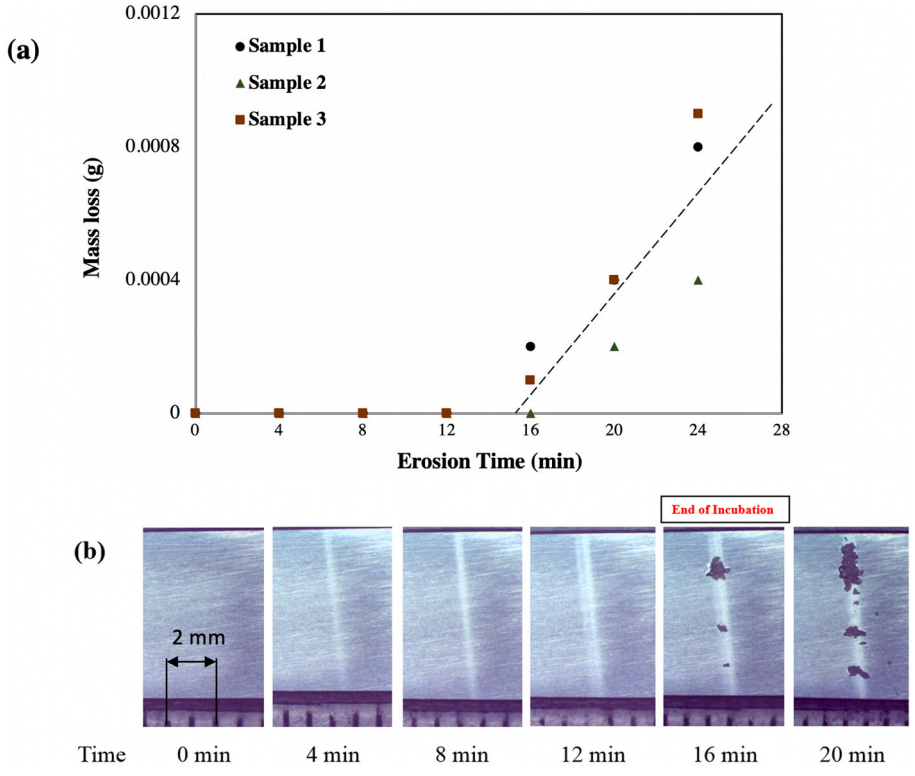

Fig. 8. Erosion Test on Ti–6Al–4V; (a) Erosion curve and (b) Optical images of the impacted area.

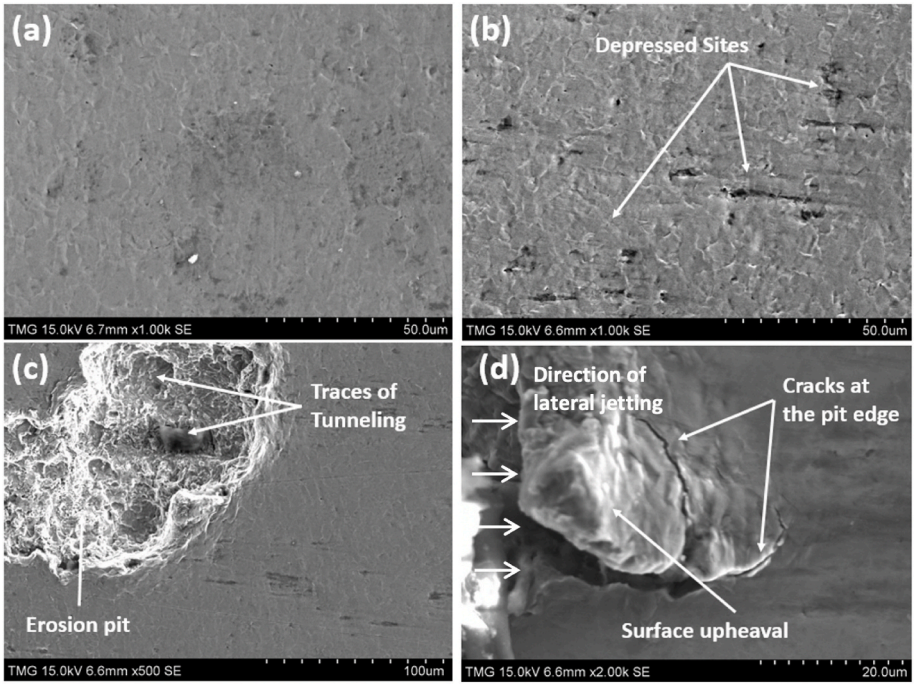

Fig. 9. SEM micrographs of impacted area at; (a) 8 min, (b) 12 min, (c) and (d) 16 min.

period (initiation of damage) can be seen as the combination of pitting and shearing of surface upheavals and irregularities (formed on the edge of erosion pits) by lateral jetting.

3.2. Evolution of hardness and roughness during the incubation period

In this work, the hardness (H_v) and average surface roughness (S_a, area roughness) of the initially polished sample were first evaluated. Then, hardness and average surface roughness were measured at 4 intervals during the incubation stage of Ti–6Al–4V. The result is shown in Fig. 10. It can be seen from Fig. 10 that hardness increases almost linearly with the exposure to droplet impacts (i.e., linear hardening behavior). The percentage of hardness increase is approximately 15%. Hardening during incubation period stage has traditionally been attributed to the accumulation of plastic strain due to the deformation caused by droplet impact [17].

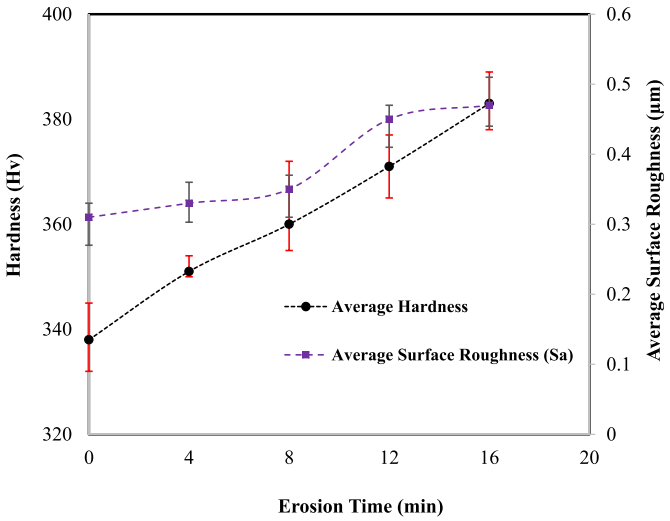

Fig. 10. Change of hardness and average surface roughness during the incubation period of Ti–6Al–4V tested at 250 m/s.

Fig. 10 also depicts how the average surface roughness changes simultaneously with hardness (i.e., roughening process) over the span of the incubation period. This increase in surface roughness comes from the interactions (i.e., the impact and spreading) of the droplets with the solid surface. It can be attributed also to the plastic deformation, which changes the topography of the impact area. Fig. 10 indicates that the magnitude of S_a increases only slightly during the first 8 min of exposure to droplet impacts. This is consistent with the microstructural observations in Fig. 9 and corresponds to the initial stages of the formation of crack networks and surface depression. Between 8 min and 12 min of exposure, a noticeable change in the average roughness occurs, possibly due to the increase in the formation of localized surface depressions and their distribution over the impact area. As the exposure to subsequent impacts continues after 12 min into the incubation period, the rate of surface roughening decreases. The overall increase in the average surface roughness towards the end of the incubation period is more than 50%.

The change in skewness during the incubation period has also been measured to understand the nature of change in surface topography due to droplet impacts. The results are shown in Fig. 11. Skewness represents the deviation of the roughness profile from symmetry. A negative value of skewness indicates that the surface is made up mainly of valleys. It can be seen from Fig. 11 that skewness maintains a negative but close to zero value until 8 min of exposure to droplet impacts. After 8 min, the value of skewness decreases drastically, coinciding with the sharp increase in average surface roughness. This suggests that the valleys in roughness profile of the test sample increase in number and depth, which confirms the formation of uniformly distributed surface depressions during the initial stages of erosion. This is supported by the work of Mahdipoor et al. [47], where roughness profile including surface depressions is captured for TiAl using atomic force microscope (AFM). Interestingly, an inflection point in skewness is seen after 12 min of exposure, which indicates a sudden shift in the rate of change in valleys formation on the roughness profile. This could be an indication of widening of the surface depressions.

The evolution of hardness and surface roughness parameters could not be accurately evaluated after the formation of uniform pitting on the surface. This is because the variation in the hardness, as well as the

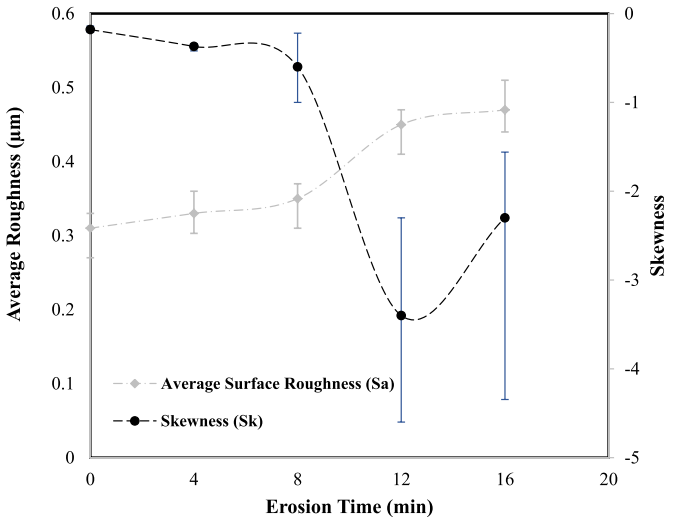

Fig. 11. Change in the average surface roughness and skewness during incubation period of Ti–6Al–4V tested at 250 m/s.

roughness parameters, is greatly affected by the surface discontinuities presented by the erosion pits, which results in a large discrepancy in the measured values.

3.3. Numerical analysis of impact stresses

In this work, finite element analysis is used to understand the influence of surface roughening on the incubation period. In particular, the aim was to investigate the effect of surface depression on impact stresses, and how this may influence the damage accumulation process. For demonstration, the temporal distributions of the maximum Von-Mises stresses in the substrate during the impact on a flat surface is shown in Fig. 12. It can be observed that the peak of the maximum stress occurs at the beginning of the impact process ($\sim 2.5 \times 10^{-8}$ sec), which is the time corresponding to the peak impact pressure. Then the maximum stress in the substrate decreases rapidly after the peak value, which also follows the distribution of the impact pressure. This temporal distribution of the maximum stress is almost the same for all the 10 simulated cases but the magnitude of the peak stress is different for each case.

Due to its importance in damage initiation, the peak values of the maximum stress of the simulated cases - as described in Table 4 - are shown in Fig. 13. For comparison, the peak of the maximum stress resulting from the impact on flat surface (which is about 570 MPa) is

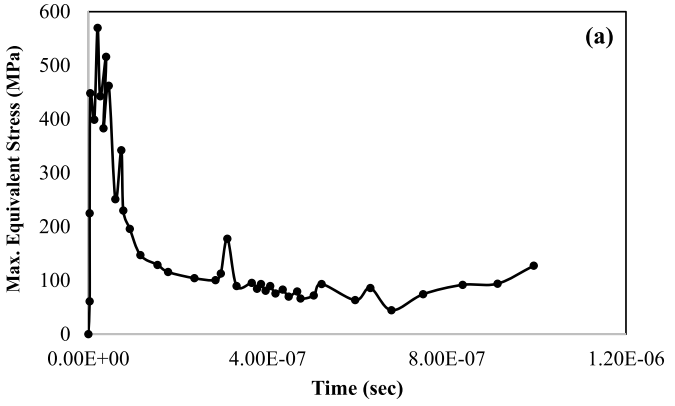

Fig. 12. Temporal distribution of the maximum equivalent (Von-Mises) stress for a compressible impact of four 600 μm spherical water droplets impinging at a velocity of 250 m/s on a flat surface.

shown as the red horizontal line. The bars represent the peak stress values of uniform depressions of varying depth for fixed width of 10, 20 and 30 μm. It can be observed from Fig. 13 that the value of the peak stress is markedly higher in all the cases of surface containing depressions compared to the smooth one. For instance, the lowest peak stress value for surface containing depressions having width of 10 μm, 20 μm and 30 μm is about 1208 MPa, 1070 MPa and 984 MPa respectively, all of them occurring when the depression depth is only 10 μm. This is approximately about 112%, 88% and 73% higher than the peak stress value in the smooth surface. It is to be mentioned that the impact process take place at high strain rate (up to 10^6 in some cases). The dynamic yield strength of the Ti–6Al–4V alloy at such high strain rate can be very high, which makes the reported finite element stresses relevant and representative. Moreover, values of the stresses in this work are used in qualitative manner and with the aim to analyze the role of the roughening process during the incubation period (rather than precisely predicting the failure of the material). More so, Gujba et al. [6] estimated the values of impact stress based on the critical impact pressure by incorporating the shock wave velocity for rigid and elastic surface at wide range of speeds (250 ms/to 350 m/s). They [6] estimated the impact stress at 250 m/s (which is the speed employed in this work) to be 658 MPa and comparing this stress value to the yield strength of Ti–6Al–4V (around 880 MPa), one could see that the material is still in the elastic range.

The influence of the depression width and depth on the resulting value of peak stress can also be studied from Fig. 13. It can be seen from Fig. 13 that, for the same depression width, the peak stress value is proportional to the depth of the surface depression. On the other hand, the peak stress value decreases with the width of the depression (expect at 30 μm depth, where all peak stress for all widths have very close values, possibly due to plateauing of the stress concentration effect). This is consistent with the trend observed with stress concentration factor (K_t) for notches with flat bottoms in semi-infinite body subjected to tension [48].

4. Discussion

4.1. Change of stresses due to roughening

The present study aims to investigate the evolution of hardness and surface roughness and their influence on the damage process during the incubation period. As mentioned earlier, at the studied impact velocity of 250 m/s, the initial droplet impact causes plastic deformation on the surface of the Ti–6Al–4V alloy. As a result, hardness of the surface increases by about 15% due to work hardening, as illustrated in Fig. 10. The increase in hardness is generally accompanied by an overall increase in erosion resistance of metallic alloys, as demonstrated in the work of Ahmad et al. [12]. If plastic strain accumulation mechanism is adopted to explain the damage accumulation during the incubation period (instead of the fatigue hypothesis [33]), this surface hardening entails that every impact cycle is required to cause slightly higher impact stress than the precedent impact cycle, such that the improved resistance can be overcome. That is, the magnitude of the impact stress should be progressively increasing during the incubation period in order to meet the progressive improvement in erosion resistance due to impact hardening. However, as the impact velocity is constant (i.e., at 250 m/s), the incident impact pressure is fixed. Therefore, it is reasonable to assume that a source of stress magnification for the same impact pressure is needed to overcome this hardening-improved-erosion resistance of the surface.

The magnification of impact stress could come directly from the roughening process, taking place simultaneously with the hardening. That is, besides hardening, the plastic deformation of the surface also results in drastic and continuous change in the surface topography. This is evidenced in the present work by the change in roughness parameters illustrated in Fig. 11 as well as the microscopic observation of the

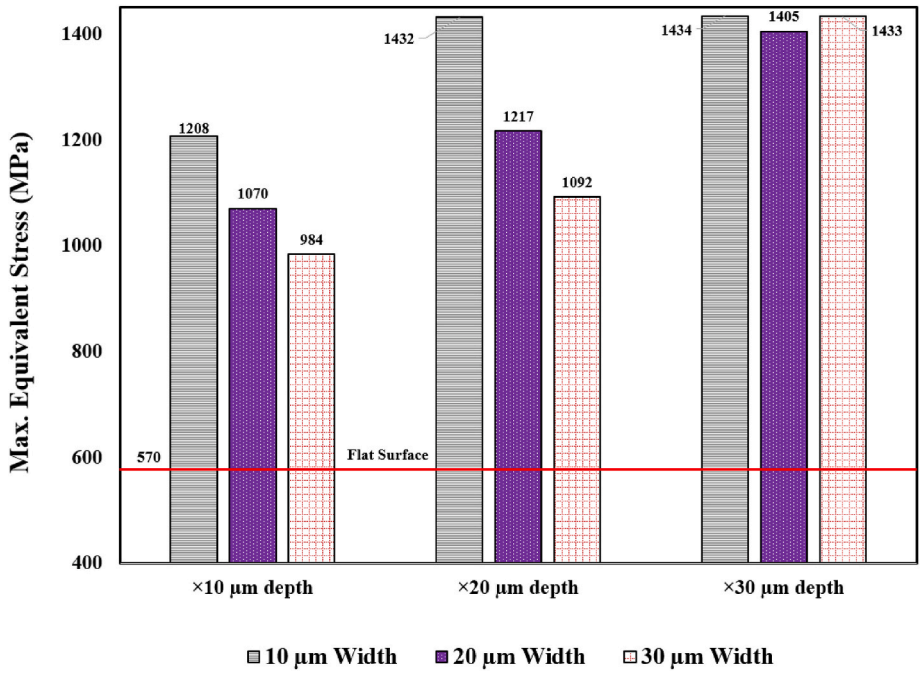

Fig. 13. Change of peak stress with Surface Condition.

formation of surface depressions (e.g., Fig. 9 (b)). Moreover, the finite element analysis presented in Fig. 13 showed that, for the same impact pressure, the peak value of the maximum impact stress for surfaces containing depressions is always higher than that of the smooth surface (i.e., 570 MPa). According to the simulated cases, the increase of impact stress due the presence of depressions can reach up to 2.5 times (i.e., ~ 1430 MPa) that of a smooth surface. This is mainly due to stress concentration caused by the presence of surface depressions.

It is to be mentioned that the yield and tensile strength of Ti–6Al–4V are around 880 MPa and 950 MPa respectively (see Table 2). This indicates that, at an impact velocity of 250 m/s, the impact pressure and the consequent stresses are not likely to cause plastic deformation on a perfectly smooth Ti–6Al–4V (i.e., threshold conditions). This is because, according to the finite element results, the maximum peak stress on a perfectly smooth Ti–6Al–4V surface is around 570 MPa, which is well below the static yield strength of the alloy. It follows that initial surface irregularities are also responsible for certain degrees of stress concentration.

Furthermore, the finite element results showed that the magnitude of stress concentration changes significantly with the change in the depression size. According to Fig. 13, the peak stress is proportional to the depth of the depression. This is important because depressed regions are likely to deepen with further droplet impacts. This is supported by the work of Huang et al. [46], who studied the mechanisms of damage initiation in Ti–6Al–4V subjected to water droplet impact loading during waterjet erosion using SEM and atomic force microscope (AFM). It was argued [46] that lateral jetting results in preferential damage to grain boundary regions, which leads to the formation of damage features such as surface irregularities and microvoids. Then, hydraulic penetration into these damage features lead to their deepening. This can further be evidenced by the change in skewness observed in this work. As mentioned, the lower the value of skewness, the deeper the valleys in the roughness profile. Roughness measurement in this work revealed that the value of skewness decreases with the exposure to droplet impacts, as shown in Fig. 11. This means that, on average, the depressed regions are likely to deepen continuously. It follows that the magnitude of stress to which the surface is subjected increases with exposure duration due to the formation and deepening of surface depressions. This trend is likely to continue until several cracks and voids merge together to form large erosion pits and craters. From a failure point of view, the cyclic increase in the magnitude of the peak stress due to surface roughening overcomes the cyclic increase in erosion resistance due to work hardening.

4.2. *Periodic polishing to prevent roughness buildup*

To test this hypothesis an additional sample of Ti–6Al–4V was tested with the same test conditions listed in Table 3 against the reference sample showed in Fig. 8 (b). Both samples were polished with 1200 grit paper before the start of the erosion test. Then, the erosion test was interrupted every 4 min and one of the samples was exposed to surface roughness homogenization (or polishing) with 1200 grit to remove the accumulated roughening, in an attempt to restore the initial surface conditions. The other sample was kept as a reference sample without polishing. The mass lost during the polishing process was less than 0.0004 g. Given the density of the Ti–6Al–4V being around 4.43 g/cm^3, this results in a volume loss of around 0.09 mm^3 and a maximum thickness loss of 3 µm over the entire surface of the sample (i.e., 8 mm × 3 mm). In most of the cases of impact treated samples, the depth of the impact hardened layer is higher than 10 µm, as demonstrated by Child et al. [49] for shot peening treatment and by Gujba et al. [42] for ultrasonic nanocrystalline modification treatment. Hence, it can be said that the polishing is done in such a way that only the roughness is removed and not the hardened layer.

Fig. 14 shows the impact area in the reference un-polished sample, the test sample before polishing, and the test sample after polishing. It can be seen from this figure that continuous polishing of the sample resulted in delaying the formation of erosion pits and resulted in a longer incubation period. This confirms that removing the rough layer from the impact area influences the stress accumulation process by eliminating the stress concentration due to the surface irregularities. This is the first time where such an experiment is done.

It is noteworthy that regularly restoring the initial surface condition alone did not completely prevent the eventual erosion of the sample as a pit eventually formed after 16 min. This is interesting because it indicates that, with slight help from the initial roughness, the direct impact pressure on the surface and the stress waves resulting from it can singlehandedly cause detectable material damage. It is possible that the stress waves may cause internal stresses beneath the surface that could

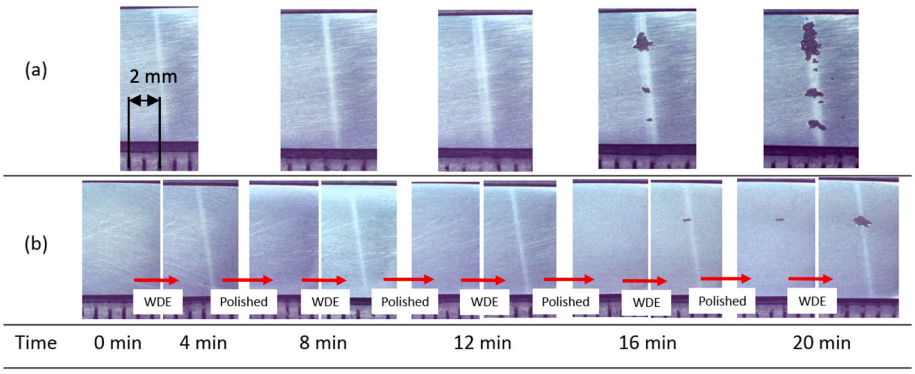

Fig. 14. Images of the impact area on the (a) reference sample, (b) sample that gets continuously polished after each test.

result in potential subsurface cracks. These cracks then accumulate into networks and lead to sudden appearance of erosion pits, as shown in Fig. 14 (b). The continuous polishing seems to eliminate or reduce the contribution of lateral jetting and stress concentration that would otherwise accelerate the damaging process.

Although the present analysis of the impact stresses is qualitative in nature, it sheds light on the role of cyclic hardening and roughening on the damage accumulation process during the incubation period. These are important factors that have never been considered in the modelling and prediction of the incubation period [23,25,50]. That is, previous studies focused only on the initial roughness and hardness values without giving much attention to the way in which these parameters evolve with exposure to impingements. For instance, the work of Ruml et al. [51] represents the only model that considered the initial surface roughness (Ra) in the prediction of the incubation period. They [51] did not, however, discussed the evolution of roughness and its role in the damage process.

It should be mentioned that the value of the peak stress and its evolution with surface depressions depend on the size of the impacting droplets [13]. Moreover, the evolution of surface depressions - caused by droplet impacts - can be viewed as a function of the mechanical properties of the surface. This is because depressed regions result from plastic deformation, which is governed by the mechanical properties and the way in which they change with exposure to impingements (i.e., hardening). As such, it can be concluded that hardening and surface roughening are crucial parameters that both need to be considered in predicting the duration of the incubation period.

5. Conclusion

In this work, the effect of hardening and surface roughening on damage accumulation during the incubation period of Ti–6Al–4V is studied. The main conclusions of this study are as follows:

- Initial droplet impingements cause plastic deformation on the impacted metal. The plastic deformation results in a steady increase in surface hardness that reach up to 15% by the end of the incubation period.
- The plastic deformation also results in formation of surface depressions that gradually deepen with continuous exposure to droplet impingements, potentially through hydraulic penetration.
- Finite element simulations of surface containing depressions of different size showed that the peak stress value is higher in rough surfaces compared to a flat one. The stress increases significantly with the depth of the depression.
- Hardening due droplet impacts results in a dynamic improvement in erosion resistance of the surface. This improvement in erosion resistance is overcome by the concentration of impact stresses due to the roughening process.
- Elimination of the roughening factor through intermittent polishing of the surface was found to increase the length of the incubation period by reducing the stress concentration.

Author agreement

As corresponding author, I, Prof. Mamoun Medraj, and all the authors confirm that:

i) The paper has not been published previously, that it is not under consideration for publication elsewhere, and that if accepted it will not be published elsewhere in the same form, in English or in any other language, without the written consent of the publisher.
ii) The paper does not contain material which has been published previously, by the current authors or by others, of which the source is not explicitly cited in the paper.
iii) The paper has been read by all the authors and the order of authors listed has been approved by all the authors.

Declaration of competing interest

The authors declare that they have no known competing financial interests or personal relationships that could have appeared to influence the work reported in this paper.

Data availability

Data will be made available on request.

Acknowledgements

The authors acknowledge the financial support received from Natural Science and Engineering Research Council (NSERC) of Canada through grant number RGPIN/06789–2018.

References

[1] Z. Zhang, T. Liu, D. Zhang, Y. Xie, Water droplet erosion life prediction method for steam turbine blade materials based on image recognition and machine learning, J. Eng. Gas Turbines Power 143 (2021), https://doi.org/10.1115/1.4049768.
[2] J. Di, S. Wang, X. Yan, X. Jiang, J. Lian, Z. Zhang, Y. Xie, Experimental Research on water droplet erosion resistance characteristics of turbine blade substrate and strengthened layers materials, Materials 13 (2020) 4286, https://doi.org/10.3390/ma13194286.
[3] A.K. Gujba, L. Hackel, D. Kevorkov, M. Medraj, Water droplet erosion behaviour of Ti–6Al–4V and mechanisms of material damage at the early and advanced stages, Wear 358–359 (2016) 109–122, https://doi.org/10.1016/j.wear.2016.04.008.
[4] C.B. Burson-Thomas, R. Wellman, T.J. Harvey, R.J.K. Wood, Water droplet erosion of aeroengine fan blades: the importance of form, Wear 426–427 (2019) 507–517, https://doi.org/10.1016/j.wear.2018.12.030.
[5] M. Ibrahim, M. Medraj, Water droplet erosion of wind turbine blades: mechanics, testing, modeling and future perspectives, Materials 13 (2020) 157, https://doi.org/10.3390/ma13010157.

[6] A.K. Gujba, M.S. Mahdipoor, M. Medraj, Water droplet impingement erosion performance of WC-based coating sprayed by HVAF and HVOF, Wear 484–485 (2021), 203904, https://doi.org/10.1016/j.wear.2021.203904.

[7] Heymann, F.J. Liquid impingement erosion. In Friction, Lubrication, and Wear Technology; J.K. Wood, R., Ed.; ASM Handbook; ASM International; Vol. vol. 18, pp. 302–312.

[8] L. Mishnaevsky, C.B. Hasager, C. Bak, A.-M. Tilg, J.I. Bech, S. Doagou Rad, S. Fæster, Leading edge erosion of wind turbine blades: understanding, prevention and protection, Renew. Energy 169 (2021) 953–969, https://doi.org/10.1016/j.renene.2021.01.044.

[9] L. Bartolomé, J. Teuwen, Prospective challenges in the experimentation of the Rain erosion on the leading edge of wind turbine blades, Wind Energy 22 (2019) 140–151, https://doi.org/10.1002/we.2272.

[10] N. Fujisawa, Liquid droplet impingement erosion on multiple grooves, Wear 462–463 (2020), 203513, https://doi.org/10.1016/j.wear.2020.203513.

[11] Z. Zhang, D. Zhang, Y. Xie, Experimental study on water droplet erosion resistance of coatings (Ni60 and WC-17Co) sprayed by APS and HVOF, Wear 432–433 (2019), 202950, https://doi.org/10.1016/j.wear.2019.202950.

[12] M. Ahmad, M. Schatz, M.V. Casey, An empirical approach to predict droplet impact erosion in low-pressure stages of steam turbines, Wear 402–403 (2018) 57–63, https://doi.org/10.1016/j.wear.2018.02.004.

[13] K. Fujisawa, M. Ohki, N. Fujisawa, Influence of surface roughness on Liquid droplet impingement erosion, Wear 432–433 (2019), 202955, https://doi.org/10.1016/j.wear.2019.202955.

[14] J. Di, S. Wang, X. Yan, L. Cai, Y. Xie, Experimental investigation on effect of surface strengthening process and roughness on water droplet erosion behavior in turbomachinery, Tribol. Int. 153 (2021), 106647, https://doi.org/10.1016/j.triboint.2020.106647.

[15] H.S. Kirols, D. Kevorkov, A. Uihlein, M. Medraj, The effect of initial surface roughness on water droplet erosion behaviour, Wear 342–343 (2015) 198–209, https://doi.org/10.1016/j.wear.2015.08.019.

[16] J. Poloprudský, A. Nag, T. Kruml, S. Hloch, Effects of Liquid droplet volume and impact frequency on the integrity of Al alloy AW2014 exposed to subsonic speeds of pulsating water jets, Wear 488–489 (2022), 204136, https://doi.org/10.1016/j.wear.2021.204136.

[17] W.F. Adler, The mechanics of Liquid impact, in: Treatise on Materials Science and Technology vol. 16, Academic Press, 1979, pp. 127–183.

[18] K. Fujisawa, Effect of impact velocity on time-dependent force and droplet pressure in high-speed Liquid droplet impingement, Ann. Nucl. Energy 166 (2022), 108814, https://doi.org/10.1016/j.anucene.2021.108814.

[19] J.E. Field, ELSI conference: invited lecture: Liquid impact: theory, experiment, applications, Wear 233–235 (1999) 1–12, https://doi.org/10.1016/S0043-1648(99)00189-1.

[20] F. Heymann, On the time dependence of the rate of erosion due to impingement or cavitation, in: Erosion by Cavitation or Impingement, 1967, https://doi.org/10.1520/STP46046S.

[21] G02 Committee *Test Method For Liquid Impingement Erosion Using Rotating Apparatus*; ASTM International;.

[22] E.F. Tobin, T.M. Young, Analysis of incubation period versus surface topographical parameters in Liquid droplet erosion tests, MPC 6 (2017) 144–164, https://doi.org/10.1520/MPC20160085.

[23] H. Slot, D. Matthews, D. Schipper, E. van der Heide, Fatigue-based model for the droplet impingement erosion incubation period of metallic surfaces, Fatig. Fract. Eng. Mater. Struct. 44 (2021) 199–211, https://doi.org/10.1111/ffe.13352.

[24] A. Thiruvengadam, S. Rudy, M. Gunasekaran, Experimental and analytical investigations on Liquid impact erosion, in: Characterization and Determination of Erosion Resistance, ASTM Special Technical Publication; ASTM International, 1970.

[25] G.S. Springer, Erosion by Liquid Impact, Scripta Publishing Co., Washington, DC, USA, 1976.

[26] M.E. Ibrahim, M. Medraj, Prediction and experimental evaluation of the threshold velocity in water droplet erosion, Mater. Des. 213 (2022), 110312, https://doi.org/10.1016/j.matdes.2021.110312.

[27] H. Rieger, The damage to metals on high speed impact with water droplets, in: Proceedings of the First International Conference on Rain Erosion and Associated Phenomena, Royal Aircraft Establishment: Meersburg, Germany, 1965.

[28] G. Hoff, G. Langbein, H. Rieger, Material destruction due to Liquid impact, in: Erosion by Cavitation or Impingement, 1967, https://doi.org/10.1520/STP46045S.

[29] N.L. Hancox, J.H. Brunton, The erosion of solids by the repeated impact of Liquid drops, Philos. Trans. R. Soc. London, Ser. A 260 (1966) 121–139, https://doi.org/10.1098/rsta.1966.0036.

[30] M. Pohl, J. Stella, Quantitative CLSM roughness study on early cavitation-erosion damage, Wear 252 (2002) 501–511, https://doi.org/10.1016/S0043-1648(02)00003-0.

[31] A.F. Mednikov, V.A. Ryzhenkov, L.I. Seleznev, A.I. Lebedeva, Studying the variation of parameters characterizing the material surface during the droplet erosion incubation period, Therm. Eng. 59 (2012) 414–420, https://doi.org/10.1134/S0040601512050072.

[32] ASM material data sheet. http://asm.matweb.com/search/SpecificMaterial.asp?bassnum=MTP641. (Accessed 11 August 2021).

[33] R.A. Shaik, M.E. Ibrahim, A.K. Gujba, M.D. Pugh, M. Medraj, On the role of strain hardening and mechanical properties in water droplet erosion of metals, Tribol. Int. 173 (2022), 107649, https://doi.org/10.1016/j.triboint.2022.107649.

[34] M.S. Mahdipoor, H.S. Kirols, D. Kevorkov, P. Jedrzejowski, M. Medraj, Influence of impact speed on water droplet erosion of TiAl compared with Ti6Al4V, Sci. Rep. 5 (2015), 14182, https://doi.org/10.1038/srep14182.

[35] V.A. Ryzhenkov, A.I. Lebedeva, A.F. Mednikov, Erosion wear of the blades of wet-steam turbine stages: present state of the problem and methods for solving it, Therm. Eng. 58 (2011) 713, https://doi.org/10.1134/S0040601511090138.

[36] M. Ahmad, M. Schatz, M.V. Casey, Experimental investigation of droplet size influence on low pressure steam turbine blade erosion, Wear 303 (2013) 83–86, https://doi.org/10.1016/j.wear.2013.03.013.

[37] Marzbali, M.; Dolatabadi, A.; Jedrzejowski, P. Fluid-solid interaction modeling of compressible droplet impact onto elastic substrates. In 21st AIAA Computational Fluid Dynamics Conference; American Institute of Aeronautics and Astronautics.

[38] M. Marzbali, Numerical Analysis of High-Speed Droplet Impingement on Elastic and Rigid Substrates, 2017.

[39] M. Marzbali, A. Dolatabadi, 2D Axisymmetric Modelling of Single Liquid Droplet Impingement at High Speeds on Thin Liquid Films in Compressible Regime, August 1 2020.

[40] M. Marzbali, A. Dolatabadi, Flow Characterization of a Water Drop Impinged onto a Rigid Surface at a High Speed and Normal Angle in the Presence of Stagnant Air at Ambient Condition, vol. 7, 2020, pp. 92–104, https://doi.org/10.11159/jffhmt.2020.009.

[41] M. Marzbali, A. Dolatabadi, High-speed droplet impingement on dry and wetted substrates, Phys. Fluids 32 (2020), 112101, https://doi.org/10.1063/5.0020977.

[42] A.K. Gujba, Z. Ren, Y. Dong, C. Ye, M. Medraj, Effect of ultrasonic nanocrystalline surface modification on the water droplet erosion performance of Ti6Al4V, Surf. Coating. Technol. 307 (2016) 157–170, https://doi.org/10.1016/j.surfcoat.2016.08.054.

[43] N. Kamkar, F. Bridier, P. Jedrzejowski, P. Bocher, Water droplet impact erosion damage initiation in forged Ti–6Al–4V, Wear 322–323 (2015) 192–202, https://doi.org/10.1016/j.wear.2014.10.020.

[44] C. Gerdes, A. Karimi, H.W. Bieler, Water droplet erosion and microstructure of laser-nitrided Ti 6A1 4V, Wear 186–187 (1995) 368–374, https://doi.org/10.1016/0043-1648(95)07153-9.

[45] J.W. Morris, N.E. Wahl, Rain erosion damage of ductile metals, in: Proceedings of the Fourth International Conference on Rain Erosion and Associated Phenomena, Royal Aircraft Establishment: Meersburg, Germany, 1974.

[46] L. Huang, J. Folkes, P. Kinnell, P.H. Shipway, Mechanisms of damage initiation in a Titanium alloy subjected to water droplet impact during ultra-high pressure plain waterjet erosion, J. Mater. Process. Technol. 212 (2012) 1906–1915, https://doi.org/10.1016/j.jmatprotec.2012.04.013.

[47] M.S. Mahdipoor, D. Kevorkov, P. Jedrzejowski, M. Medraj, Water droplet erosion mechanism of nearly fully-lamellar gamma TiAl alloy, Mater. Des. 89 (2016) 1095–1106, https://doi.org/10.1016/j.matdes.2015.10.077.

[48] W.D. Pilkey, D.F. Pilkey, Z. Bi, Peterson's Stress Concentration Factors, John Wiley & Sons, 2020, ISBN 978-1-119-53251-4.

[49] D.J. Child, G.D. West, R.C. Thomson, Assessment of surface hardening effects from shot peening on a Ni-based alloy using Electron backscatter diffraction techniques, Acta Mater. 59 (2011) 4825–4834, https://doi.org/10.1016/j.actamat.2011.04.025.

[50] D. Borello, P. Venturini, S. Gabriele, M. Andreoli, New Model to Predict Water Droplets Erosion Based on Erosion Test Curves: Application to On-Line Water Washing of a Compressor, American Society of Mechanical Engineers Digital Collection, November 5 2019.

[51] Z. Ruml, F. Straka, A new model for steam turbine blade materials erosion, Wear 186 (1995) 421–424.